Effect of crystallographic texture on pair distribution function analysis in engineering materials

Acta Materialia 310 (2026) 122122

Contents lists available at ScienceDirect

Acta Materialia

journal homepage: www.elsevier.com/locate/actamat

Effect of crystallographic texture on pair distribution function analysis in engineering materials

Monika Rolinska [a,*], Lewis R. Owen [b], Yuanpeng Zhang [c], Peter Hedström [a], Matthew G. Tucker [c]

[a] Department of Materials Science and Engineering, KTH Royal Institute of Technology, Brinellvägen 23, Stockholm 100 44, Sweden
[b] School of Chemical, Materials and Biological Engineering, University of Sheffield, Sir Robert Hadfield Building, Mappin Street, Sheffield S1 3JD, United Kingdom
[c] Oak Ridge National Laboratory, Neutron Scattering Division, Oak Ridge, TN 37831, United States

ARTICLE INFO

Keywords:
Short-range order
Short-range ordering
Texture
Pair-correlation function
Diffraction

ABSTRACT

Physical properties of alloys are known to be affected by local order on the atomic scale; however, since this structural feature appears on sub-nanometer to nanometer scale, characterization of it is inherently challenging. Interest in local order in metallic systems has increased in recent years, driven by the development of increasingly compositionally complex alloys and observation of phenomena that cannot be explained by microstructural changes alone. One way to study local order is through the total scattering technique, an extension of powder diffraction where Bragg scattering and diffuse scattering are analyzed, often primarily through the pair distribution function. The calculation of a pair distribution function assumes an ideal powder with randomly oriented crystallites (i.e., without texture), which is rarely the case for conventionally processed engineering materials. Texture has numerically been shown to affect an arbitrary pair distribution function, but the effect has not been explored in depth across different alloy systems. In this work, we investigate the effect of texture on pair distribution functions for typical engineering materials through simulations, validate the simulation results with experimental data, and investigate potential artificial short-range order effects that may arise in large box models when texture is present. We show that different types of texture introduce perturbations in real space, which in turn affect model fitting within the Reverse Monte Carlo modelling framework. Based on this work, we conclude that samples for which the presence of texture cannot be excluded, through experimental setup or data reduction methods, are not suitable for standard PDF analysis.

1. Introduction

Local order phenomena have been observed for numerous metallic material systems including nickel-base [1], iron-base [2,3] and high-entropy alloy systems [4–6]. Short-range order has a significant impact on important functional and mechanical properties of metals, and can also influence phase transformation kinetics [7]. Local order phenomena in alloys have been studied with various methods since the discovery of the complex state (K-state) in Ni-Cr alloys and other systems [8]. It was found that the resistivity of an alloy was affected by the heat treatment temperature even though there was no observed changes in the microstructure. This change was attributed to a local order state that was structurally distinct from both the random and the phases with long-range order found in the phase diagram. Historically, progress in studies of local order has been hindered by the inherent difficulty associated with characterizing features on the near-atomic scale. Recently, however, interest in this area has resurged driven primarily by the need to investigate local structural features such as local chemical order but also local lattice strains in high-entropy alloys [4].

Local order can be characterized by different techniques, such as atom probe tomography, transmission electron microscopy, Mössbauer spectroscopy, X-ray absorption spectroscopy, and scattering techniques, each method having its own unique advantages and disadvantages. One method for analyzing local order phenomena in alloys is total scattering, combined with pair distribution function (PDF) analysis [9]. The total scattering technique is a powder diffraction technique in which both the average information and the local information are analyzed simultaneously by including both the Bragg scattering and the diffuse scattering. The measured structure factor $F(Q)$ can be Fourier transformed into real space to give the PDF, facilitating analysis of the local structural

* Corresponding author at: Department of Physics and Astronomy, Chalmers University of Technology, Kemigården 1, 412 96, Gothenburg, Sweden.
E-mail address: rolinska@chalmers.se (M. Rolinska).

https://doi.org/10.1016/j.actamat.2026.122122
Received 15 September 2025; Received in revised form 9 March 2026; Accepted 13 March 2026
Available online 17 March 2026

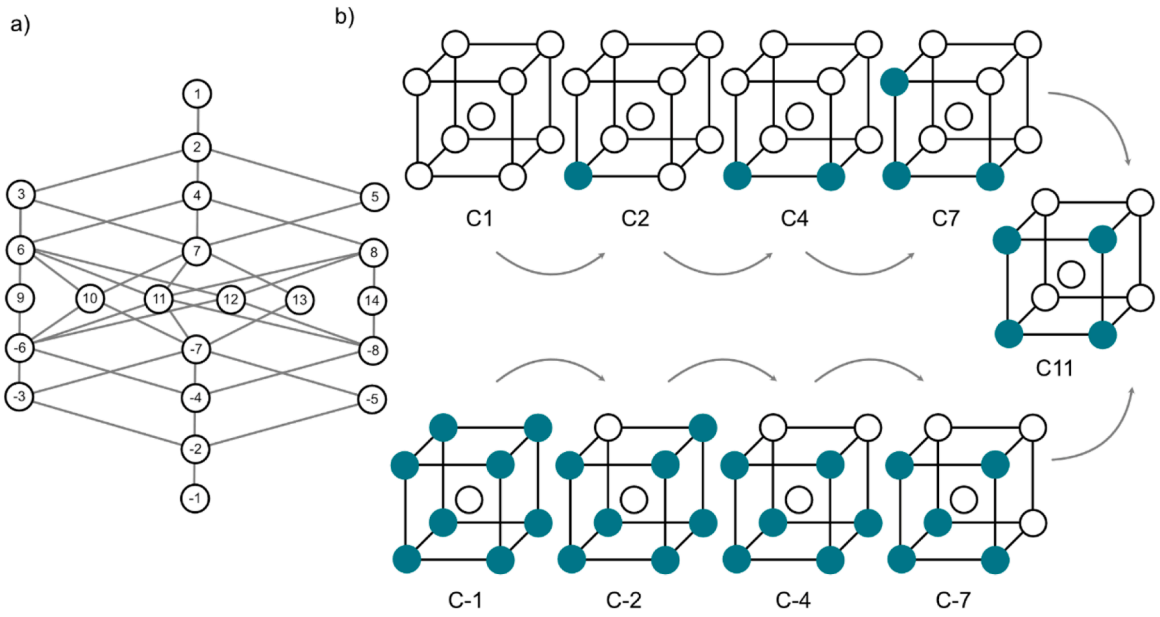

Fig. 1. (a) Schematic illustration of degradation pathways showing relations between Clapp configurations present for the bcc system (b) A selection of possible pathways between C1 (or C-1) and the C11 configuration where the white and the colored atom are atoms of type A and B respectively.

features encoded in the diffuse scattering portion of the $F(Q)$. The area of the PDF peaks is directly related to the occupancy of an atomic species at a distance from a given atom in the material, and the method gives an intuitive way to interpret interatomic distances directly from the data. Total scattering is a method that can be applied to a wide range of materials, and the local order can be analyzed by either "small box" modelling techniques, also referred to as real-space Rietveld, or by "large box" techniques, including Reverse Monte Carlo (RMC) modelling [10]. The small box techniques typically use a single unit cell as input and the structure is refined to fit the experimental data with a few degrees of freedom, whereas the large box techniques use supercells with many thousands of atoms that are allowed to move to minimize the difference to experimental data. The complex local behavior of alloys calls for analysis through the large box modelling scheme to capture both short-range and the intermediate-range order [9].

Being inherently a powder diffraction technique, the assumption in total scattering is that the measured sample is a perfect crystallographic powder which scatters isotropically, without preferred orientation of the crystallites. In recent successful total scattering work on alloys, the metal powders have been produced by gas and water atomization [4], filed, or crushed to a powder [6,11]. However, since the local order is highly dependent on the metallurgical history of the alloy [12–14] and plays a critical role in governing phenomena such as phase transformations [7,15,16], it is essential to study alloys that have undergone conventional bulk processing. This is because the state of these materials might differ compared to atomized powders, for example in regards to microsegregations [17,18], which will affect the PDF [19]. A major challenge in studying local order in bulk alloys is preferential alignment of crystallites (texture), which might develop as a result of, for example, rolling or recrystallization [20], and may also arise in powder metallurgy after sintering [21]. Texture in materials might be desired, for example for improved formability or magnetic properties, or undesired, leading to an increase in localized strain and premature failure of a component [22].

The role of texture on PDF analysis has historically been overlooked, but has recently been treated mathematically and numerically [23–25]. Both Cervellino and Frison [24] and Gong et al. [25] showed that introducing texture by manipulation of different spherical harmonics textural components influences the PDF by altering the relative intensity of the peaks. This will influence analysis of the data using both the small box and the large box approaches. For example, for a large box model, this might lead to artificial local order effects when trying to fit the PDF of an alloy with different contrast between the coherent scattering lengths of the atomic species, as the model will swap atoms to fit the intensities that have been altered by the texture. In this paper, we investigate the role of common textures for engineering materials on the PDF through simulations and use experimental results to qualitatively show the effect on a body centered cubic alloy. Finally, we explore how texture affects RMC-based model fitting for a set of chosen structures and compositions.

2. Theoretical background

2.1. Descriptions of local order in alloys

The classical way of describing short-range order in alloys is by means of the Warren-Cowley short-range order parameter α defined for the n:th coordination shell by

$$\alpha_n^{AB} = 1 - \frac{P_n^{AB}}{c_B} \tag{1}$$

Where P_n^{AB} is the probability of finding atom B in the n:th coordination shell of atom A and vice versa for P_n^{BA}, and c_A and c_B are the concentrations of atom A and B, respectively. Thus, for a random alloy $\alpha = 0$, whereas α takes on positive values if the atoms are clustered and negative values if the atoms are ordered.

Another way to describe local order in alloys, which preserves the type of structural motifs and thus the type of local order, is by analysis of so-called Clapp configurations [26,27]. Clapp configurations consider the different combinations in which atoms can be arranged in a binary system for a cubic unit cell, and reduces them to a set of configurations with respect to symmetry. The resulting Clapp configurations show distinct types of order in a cell; by identifying Clapp configurations that are enhanced relative to those expected in a random configuration, key structural motifs can be identified [9]. There are 22 Clapp configurations for the body centered cubic (bcc) system and 144 combinations for the face centered cubic (fcc) system. For the full list of configurations, the reader is referred to Ref. [27].

The configurations can be linked through degradation pathways,

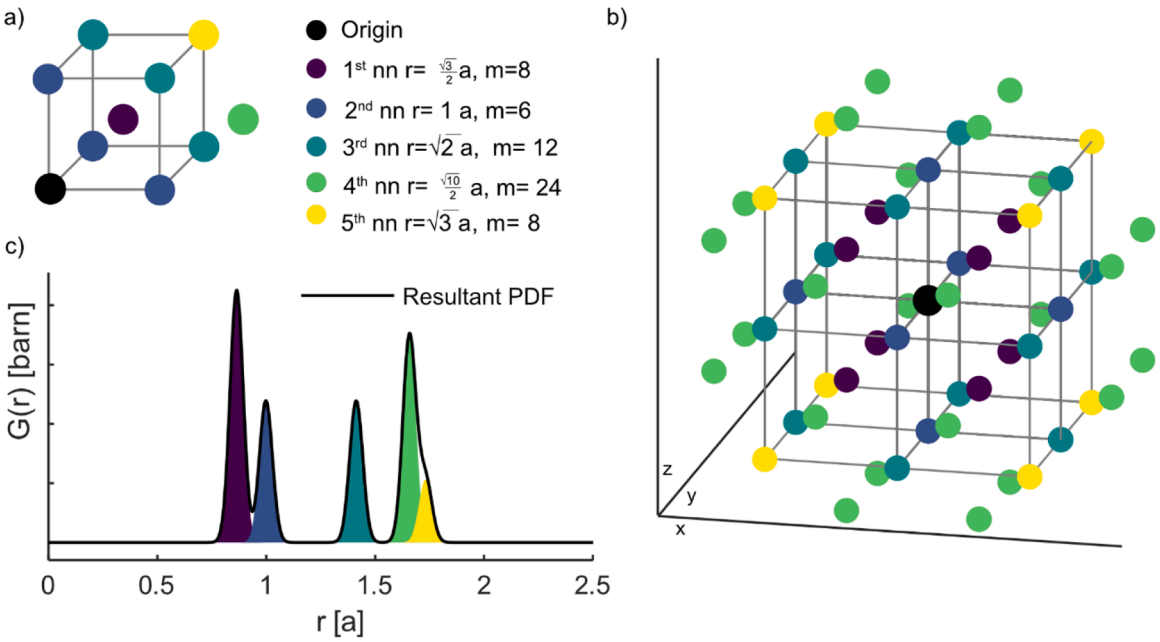

Fig. 2. Schematic illustration of the PDF (a) Visualization of coordination shells around an atom in a single bcc unit cell (b) Visualization of coordination shells including the multiplicities (c) The resulting PDF.

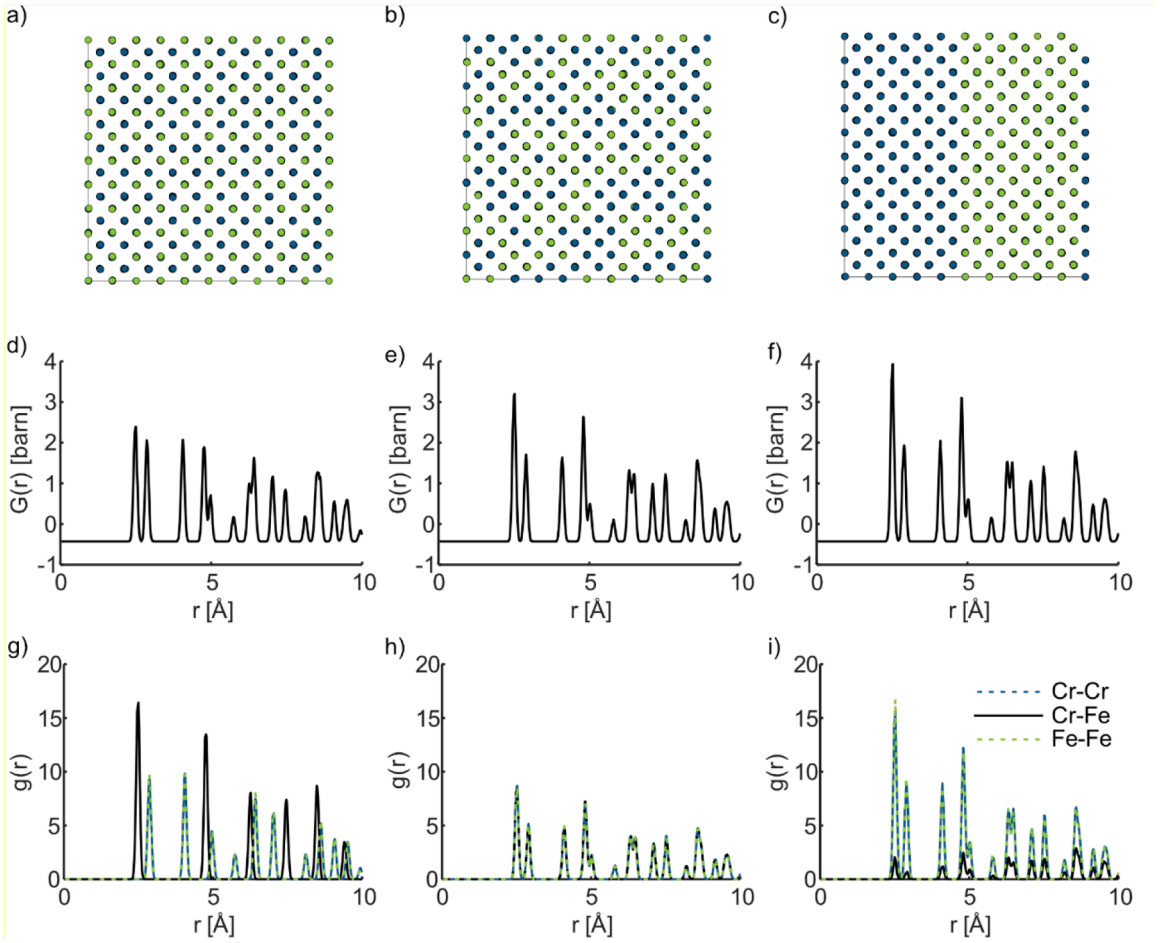

Fig. 3. Simulated large boxes and their corresponding neutron PDFs with partials for different structures in the Fe0.5Cr0.5 system, where the atoms have a small Gaussian displacement applied to mimic thermal vibrations. (a), (d) and (g) B2 type ordered structure (b), (e), (h) random bcc structure with shared sites (c), (f), i) fully phase separated system where all equal atoms are clustered, showing Fe and Cr on different sides of the box.

where the relation between the different configurations (by adding or removing an atom from the structure) is shown in Fig. 1. The full degradation diagram is presented in Fig. 1 a and an example of possible paths between C1 and C11 is presented in Fig. 1 b.

2.2. Total scattering and the pair distribution function

In a neutron diffraction experiment, following the definitions summarized by Keen [28] which will be used throughout this work, the total differential cross section $\frac{d\sigma}{d\Omega}$ relates to the total scattering function $F(Q)$ by

$$\frac{1}{N}\frac{d\sigma}{d\Omega} = F(Q) + \sum_{i=1}^{n} c_i \bar{b}_i^2 \tag{2}$$

And to the reduced structure factor $S(Q)$ by

$$S(Q) - 1 = \frac{F(Q)}{\left(\sum_i c_i \bar{b}_i\right)^2} \tag{3}$$

where Ω is the solid angle, c_i and $\bar{b}_i$ are the concentration and coherent scattering length of atomic species i, n is the total number of atomic species in the system, and N is the total number of atoms in the system. The PDF $G(r)$ is the Fourier transform of the $F(Q)$ given by

$$G(r) = \frac{1}{(2\pi)^3 \rho_0} \int_0^\infty 4\pi Q^2 F(Q) \frac{\sin Qr}{Qr} dQ \tag{4}$$

where Q is the magnitude of the momentum transfer, ρ_0 is the average number density of the structure, and r is the real-space interatomic distance. In practice, we cannot measure up to an infinite momentum transfer, but to suppress termination ripples in the Fourier transform it is important to collect data on an instrument with sufficient Q range, which often is a spallation neutron source or a synchrotron generating high-energy X-rays. The PDF is a weighted histogram of the interatomic distances defined by

$$G(r) = \sum_{ij} c_i c_j \bar{b}_i \bar{b}_j \left(g_{ij}(r) - 1\right) \tag{5}$$

where c and b have been defined previously and $g_{ij}(r)$ is the partial pair distribution function (also referred to as partial) for the i-j atom pair defined by

$$g_{ij}(r) = \frac{n_{ij}(r)}{4\pi r^2 c_i \rho_0 dr} \tag{6}$$

where n_{ij} is the number of type-j atoms with the distance r to $r+dr$, from the atom of type-i. The rest follows the definition above. Representations of the PDF vary including different forms of scaling, and the PDF might alternatively be used in its r-scaled form $D(r)$:

$$D(r) = 4\pi r \rho_0 G(r) \tag{7}$$

The PDF can be visualized for a bcc system according to Fig. 2, where Fig. 2 (a) is a representation of the atoms at different distances in a single unit cell, Fig. 2 (b) is the representation of the atoms in a supercell showing the varying number of atoms in each coordination shell (m), and Fig. 2 (c) is the resultant PDF where the area under each peak corresponds to the number and type of atoms at a given distance. An example of how different types of order affect the PDF is visualized for an equiatomic $Fe_{0.5}Cr_{0.5}$ system in Fig. 3 with corresponding partials. The relative intensities of the peaks change due to the different arrangement of the atoms with different coherent scattering lengths (Fig. 3 d–f). The differences can be observed from inspection of the partials (Fig. 3 g-i). The ordered structure partials clearly show how the atoms are occupying different coordination shells (Fig. 3 g). By contrast, for the theoretical Fe/Cr phase separated structure, the Fe-Cr pair has a very low prevalence as it is confined to the interface region which is small compared to the bulk (Fig. 3 i).

2.2.1. Reverse Monte Carlo modelling

One approach to fitting total scattering data through large box modeling is using the RMC technique implemented in software such as RMCProfile [29,30]. In RMC modelling, the algorithm moves atoms randomly within a box with thousands of atoms (move types include translations and swaps) accepting moves that improve the fit to the experimental data used as input as well as a small portion of moves that worsen the fitting according to the Boltzmann statistics (in order to avoid the system being trapped in local minima). Multiple types of experimental datasets can be included, and different weighting can be applied to each dataset to build a final model that best reflects all input data sets. The RMC algorithm will move atoms in the box according to user-imposed constraints to minimize the χ^2_{RMC} agreement value, which is a sum of the individual χ^2 values for each included dataset according to the definition below, where σ_i is the weighting parameter assigned to the dataset.

$$\chi^2_{dataset} = \sum_i \frac{\left(y_i^{obs} - y_i^{calc}\right)^2}{\sigma_i^2} \tag{8}$$

$$\chi^2_{RMC} = \sum_n \chi^2_{dataset,n} \tag{9}$$

To avoid getting stuck in a local minimum, allowing the model to converge towards a global minimum, the algorithm allows for a fraction of bad moves, increasing the χ^2 with probability

$$P = \exp\left(-\frac{\Delta\chi^2}{2}\right) \tag{10}$$

The resulting box can be analyzed to extract the Warren-Cowley parameters for specific coordination shells, but also to gain information about the relative frequency of specific Clapp configurations and these can be statistically analyzed to calculate enhancement factors (EFs), which indicate how much more frequently the configuration appears compared to what would be expected in a random box [9]. The probability of a Clapp configuration is a function of the composition of the alloy, the unit cell symmetry and the multiplicity of the configuration. The *EF* can then be calculated from a binomial distribution as

$$EF = \frac{n^*_{CC} - \mu_{CC}}{\sigma_{\mu_{CC}}} \tag{11}$$

Where n^*_{CC} is the observed number of a certain Clapp configuration in the box, μ_{CC} is the expected number of a certain Clapp configuration in the box, and $\sigma_{\mu_{CC}}$ is the standard deviation of the configuration for the box.

In-depth analysis of the box configurations is key to understanding local order phenomena in materials. To extract meaningful information from the model, it has been shown that along with physical constraints (for example bond lengths or potentials), careful data preparation is essential as incorrect (non-absolute) scaling, offsets, or inadequate resolution correction will potentially lead to local order artifacts in the box [31]. All these artifacts are introduced by intensity variations that are not accounted for in the model; for example, an inaccurate resolution function causes a decay in the intensities from low to high-r resulting in atoms with higher scattering length density to move to low-r to account for this intensity variation, resulting in artificial clustering. Since preferred orientation causes systematic increases and decreases of intensity of the $F(Q)$, it is important to investigate whether this induces any artificial order effects while analyzing the PDF.

2.3. Texture

Preferred orientation of crystallites, also referred to as crystallo-

Table 1
Summary of common textures in bcc and fcc materials.

bcc		fcc	
Common texture fiber components			
α fiber	<1 1 0> || RD; {1 1 0}<1 1 0> to {1 1 1}<1 1 0>	α fiber	{1 1 0}<-1 1 2> to {1 1 0}<0 0 1>
γ fiber	{1 1 1}|| ND; {1 1 1}<1 1 0> to {1 1 1}<1 1 2>	β fiber	{1 1 2}<1 1 -1> to {1 1 0}<-1 1 2>
Common texture components			
Goss	{1 1 0}<0 0 1>	Goss	{1 1 0}<0 0 1>
Cube	{1 0 0}<0 0 1>	Cube	{1 0 0}<1 0 0>
		Copper	{1 1 2}<1 1 -1>
		Brass	{1 1 0}<-1 1 2>
		Taylor	{4 4 11}<11 11 -8>
		S	{1 2 3}<6 3 -4>

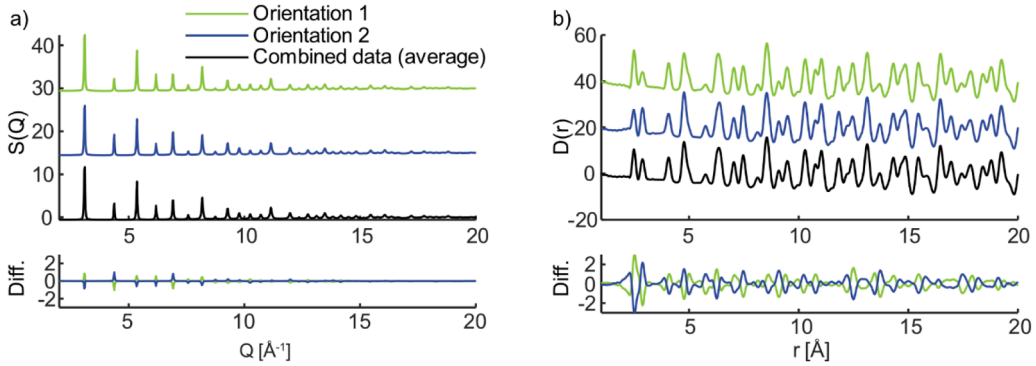

Fig. 4. (a) Reduced structure factor $S(Q)$ presented for two sample orientations in the beam, plotted together with the average of the two orientations. The difference plot shows the comparison to the average structure. (b) Pair distribution function $D(r)$ for the two orientations and an average, merged dataset, where the difference plot shows a comparison of the two measured orientations with the average structure.

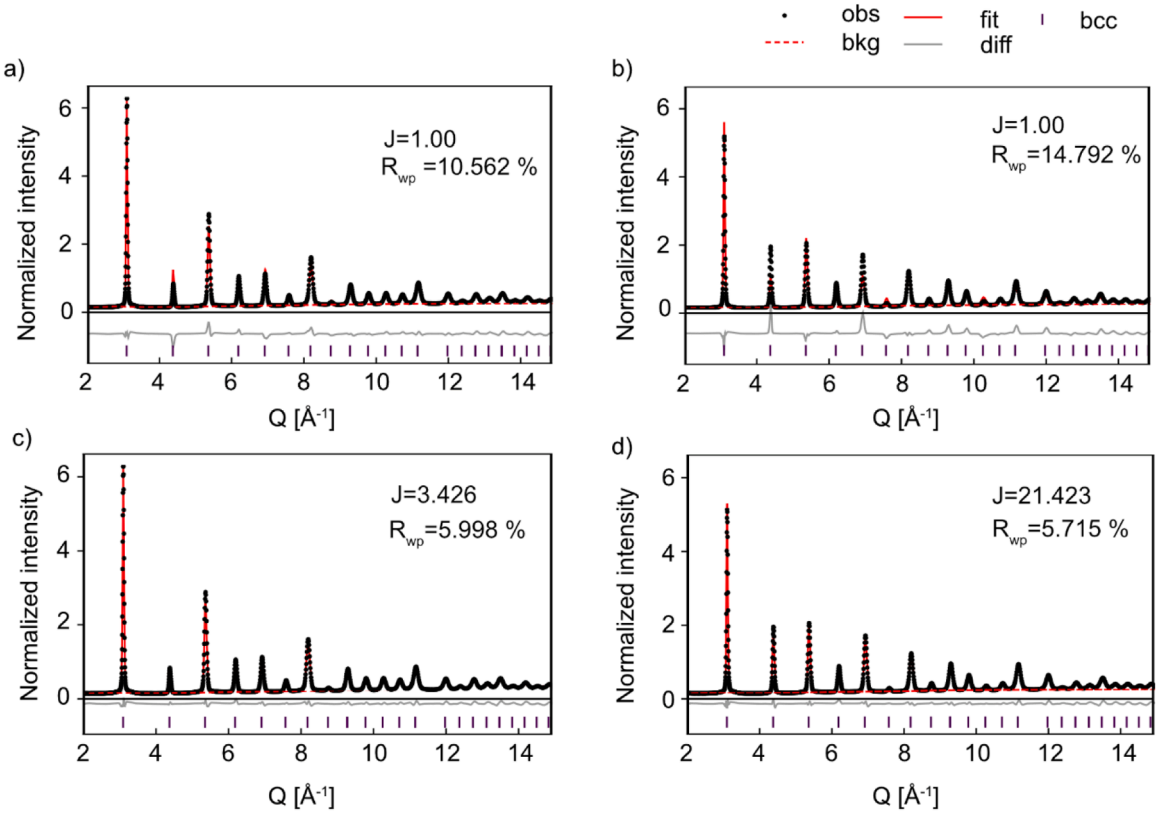

Fig. 5. Results of Rietveld refinement of a bcc structure, where (a) and (b) show the fits without fitting texture for orientation 1 and 2, respectively and (c) and (d) show the fits with texture fitted with a 16-th degree spherical harmonics expansion.

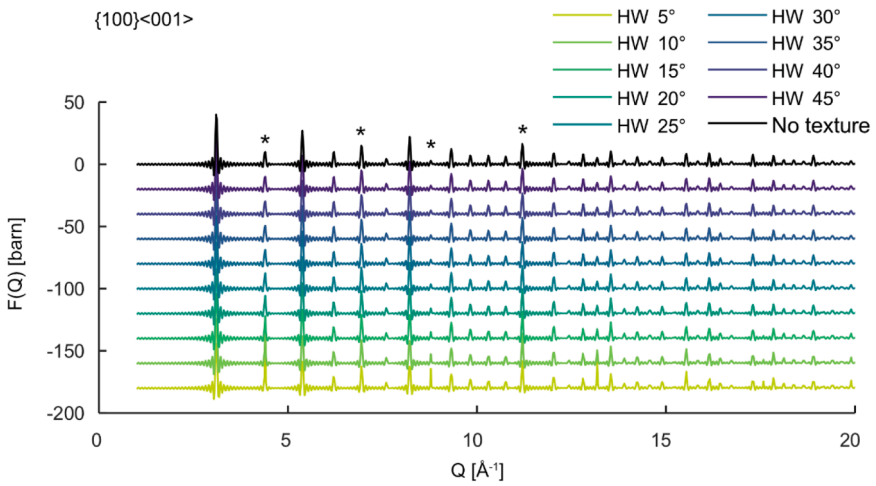

Fig. 6. The effect of the applied texture on the structure factor $F(Q)$ for increasingly sharp {100}<001> texture. A set of chosen reflections on which the intensity increase is particularly apparent is marked with an asterisk (*). The ripples around the peak positions are an effect of the finite size of the box used for calculating the structure factor, but they do not create any additional ripples in the PDF.

graphic texture, can be described by the volume fraction of different orientations of the crystallites in a volume. The orientation of a crystal K_A can be described with respect to a reference frame K_B (for example sample geometry) with rotation around three axes according to the Bunge convention [32] (and the same is true reciprocally, where the orientation of the sample K_B can be described in terms of rotation around three axes with respect to the crystal orientation K_A). The rotation is conventionally expressed in terms of rotation angles, commonly expressed with Euler angles $\varphi_1, \Phi, \varphi_2$. The orientation can be generally described for each point in the volume with coordinates x, y, z by

$$t = t(x,\ y,\ z) \tag{12}$$

If the rotation is expressed in Euler angles, this means that each coordinate needs to be defined by

$$\varphi_1 = \varphi_1(x,y,z); \Phi = \Phi(x,y,z); \varphi_2 = \varphi_2(x,\ y,\ z) \tag{13}$$

To simplify this expression for practical use, it is possible to describe the orientation distribution function (ODF) $f(t)$ for a volume V with a certain orientation by

$$\frac{dV}{V} = f(t)dt \tag{14}$$

The orientation distribution function can be developed in a series of spherical harmonics

$$f(t) = \sum_{l=0}^{\infty} \sum_{m=-l}^{+l} \sum_{n=-l}^{+l} C_l^{mn} Y_l^{mn}(t) \tag{15}$$

This function must fulfill both sample symmetry and crystal symmetry conditions. During Rietveld refinement of diffraction data, the texture can be fitted using generalized spherical harmonics. However, it is important to note that due to Friedel's law, which states that diffraction patterns are centrosymmetric, and equivalency of $I(hkl)$ and $I(\overline{hkl})$, only even order harmonics can be derived from diffraction measurements [33].

The ODF can be stereographically projected onto a 2D space, generating a pole figure often used in interpretation of texture data. However, to be able to obtain an ODF from experimentally measured data, multiple measurements are required as the detector coverage is limited. Details regarding experimental characterization of texture using scattering-based techniques are found in Ref. [34] with extensive descriptions for neutron ToF measurements in [35].Depending on how well aligned the crystallites are, the texture will be described in terms of sharpness, related to width of the spot projected onto the pole figure and the pole density, a sharp texture (low half-width of the peak) means the crystallites are more aligned. The texture strength is sometimes also described by the J-index defined as

$J = \int f^2(t)dt$. Thus, integrating the ODF enables us to evaluate the J-index which will be equal to 1 for a random distribution and reach increasing values as the texture becomes sharper in a specimen ($J = \infty$ for a single crystal).

In metallurgy, the texture components are often described with respect to the rolling direction defining an orthogonal system with rolling direction (RD), transverse direction (TD) and normal direction (ND) as system coordinates, where the texture is often expressed in Miller notation by $\{hkl\}\langle uvw\rangle$ where the {hkl} defines the lattice plane parallel to the plane of the sheet and the <uvw> is parallel to the rolling direction [36] (although there are multiple alternative ways to represent texture) [32]. A selection of common texture components for bcc and fcc materials are presented in Table 1.

3. Case example of experimentally observed texture effects on the pair distribution function

A sample of Fe-45wt%Cr (Fe-46.5Cr-0.53Si-0.08Mn-0.03Ni-0.001C at.%) was cut to a bar shape with approximate size of 3 × 3 × 40 mm, deformed and recrystallized under flowing argon gas at 1100°C. The sample was then subjected to another short heat treatment at 700°C for five minutes. The sample was cut and ground to final dimensions of approximately 2 × 2 × 40 mm.

Neutron total scattering measurements were performed for two different orientations of the sample, where it was rotated 90° between the measurements to investigate any orientation dependence on the scattering pattern caused by preferred orientation in the sample. The measurements were performed at the Nanoscale Ordered Materials Diffractometer (NOMAD) at the Spallation Neutron Source, Oak Ridge National Laboratory, Oak Ridge, Tennessee. NOMAD is a high-flux, medium resolution time-of-flight (ToF) diffractometer covering a Q-range of 0.04-100 $Å^{-1}$ [37],], where a practical Q-range typically used is 0.5-30 $Å^{-1}$. Data reduction was performed using the single-bank reduction mode, where the scattering patterns from all the physical detectors are merged (i.e., summed) together after the calibration, pixel masking and unit conversion to Q-space. This merging yields a single total scattering pattern instantaneously. The benefit of this approach is using as much of the available data as possible, but the downside is that the different resolution and peak shape from physical detectors with different scattering angle potentially can make the instrument resolution effect difficult to handle. This may affect the data fitting especially in

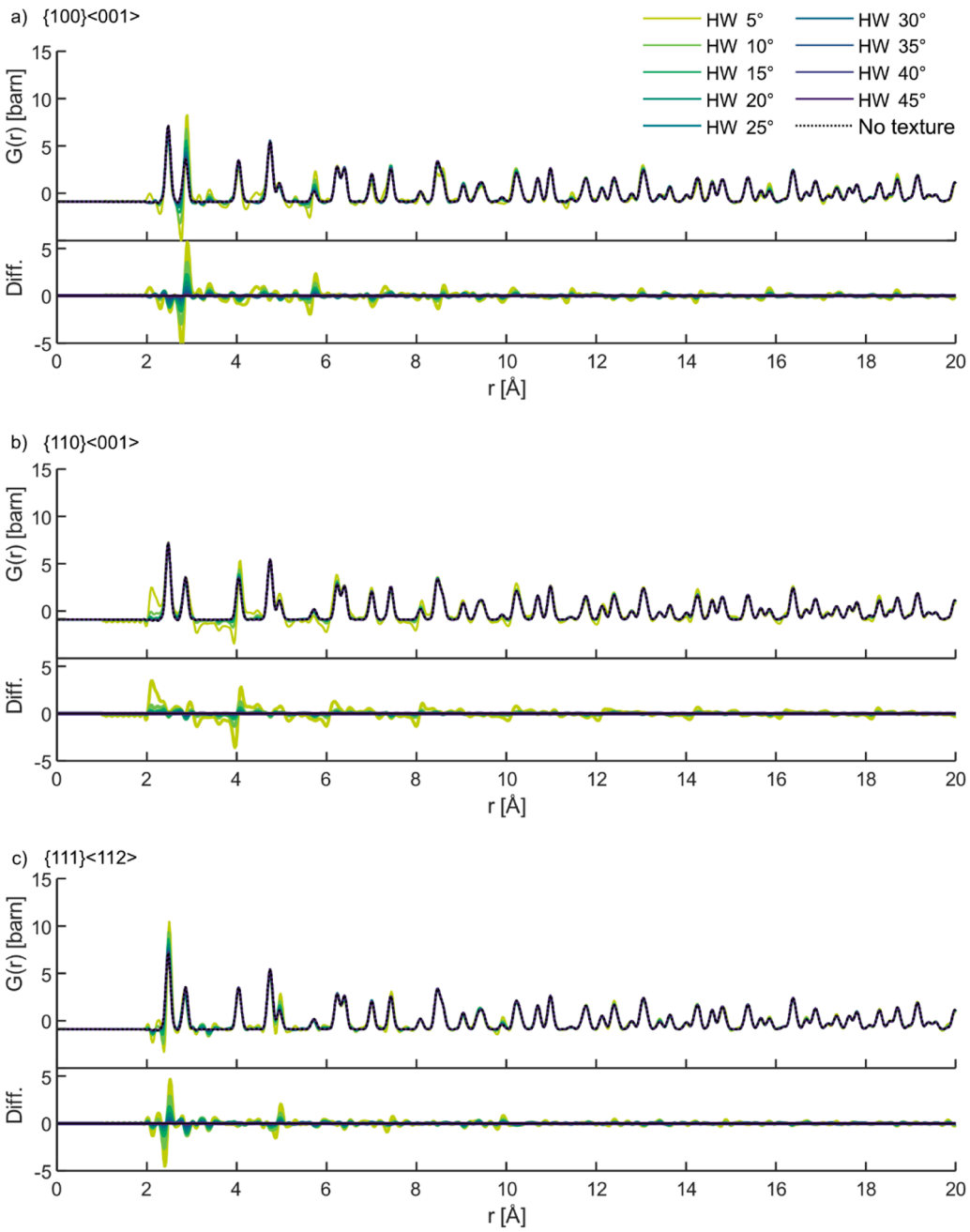

Fig. 7. Effects of different texture components on the PDFs of a bcc material (a) {100}<001> (b){110}<001> (c) {111}<112>.

Table 2
Scattering coefficients for $Fe_{0.5}Cr_{0.5}$.

Composition	Self-scattering (barn)	Faber-Ziman coefficient (barn)	Partials (barn)
$Fe_{0.5}Cr_{0.5}$	0.601	0.428	Fe-Fe=0.223 Fe-Cr=0.172 Cr-Cr=0.033

real-space when one needs to approach the high-*r* region for the fitting. This is not an issue for qualitative analysis of the data which is the aim of this paper, and the method is thus deemed suitable for this purpose. During the data treatment, the instrument background and sample environment are subtracted and the data is put on an absolute scale by normalization to a vanadium standard.

The reduced structure factor $S(Q)$ for the two different sample orientations, compared to an average structure where data for both orientations is merged, is shown in Figure a. The different relative peak intensity is evident when compared with the average structure, clearly showing that the sample is textured and that this texture is not averaged out during the merging of the detectors. The PDF presented in Fig. 4b, where the different orientations again are shown together with an average, clearly shows changes in relative intensities of the peaks depending on the sample orientation, confirming the simulation results.

To qualitatively indicate the difference in orientation Rietveld refinement was performed using the GSASII software [38] and texture was fitted using a sixteen degree spherical harmonics expansion gives a best fit of $J = 3.487$ for orientation 1 and $J = 21.423$ for orientation 2, presented in Fig. 5. While refining texture for the average structure, using both detector banks, the texture coefficient dropped to $J = 2.248$, showing that rotation could mitigate some texture effect in this case but using only two directions did not fully suppress the influence of texture.

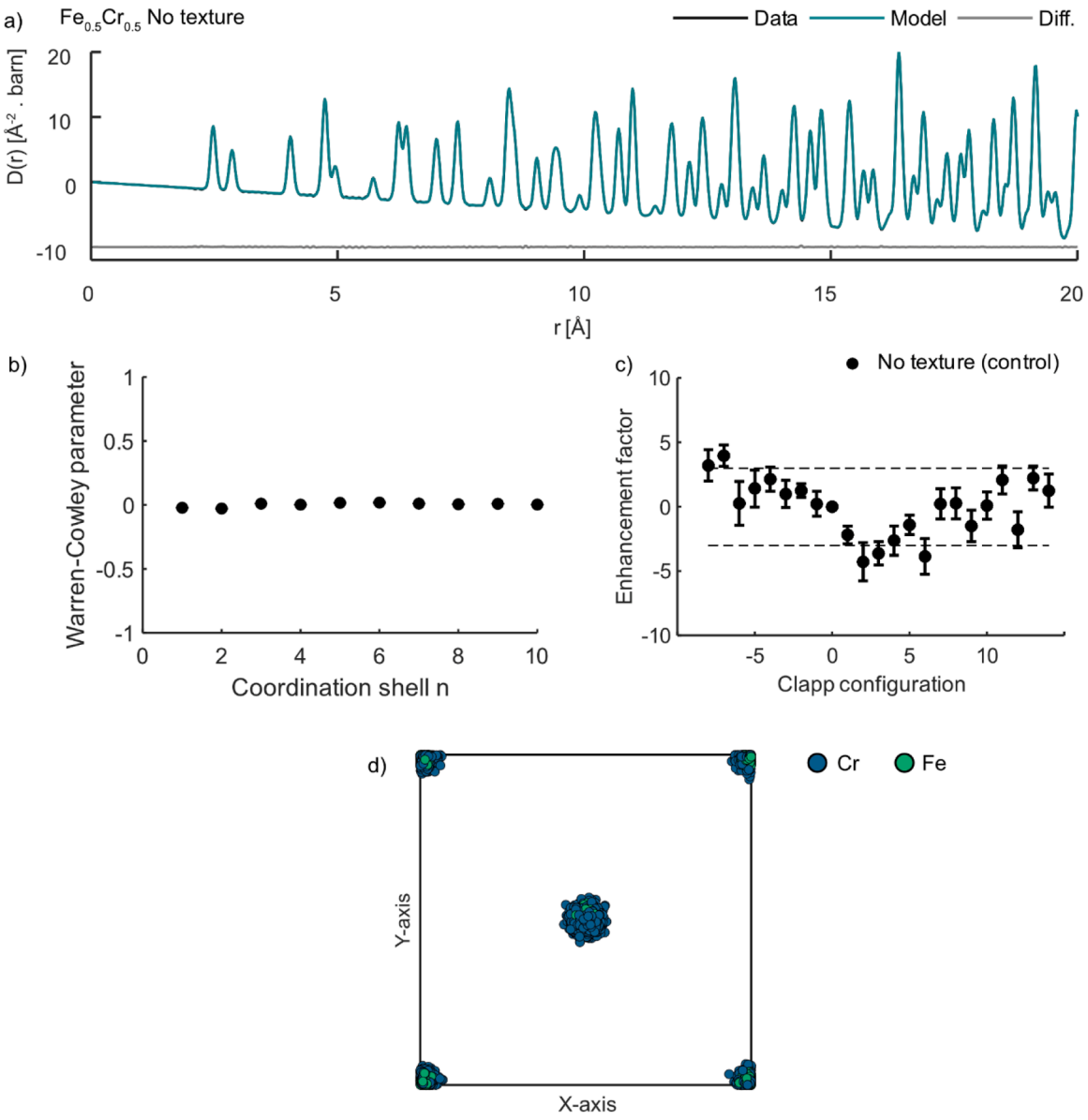

Fig. 8. Results from a control run fitting a 16 000 atom supercell of Fe0.5Cr0.5 to simulated PDF data. (a) Shows the fit to the $D(r)$, (b) shows the average distribution of Warren-Cowley parameters for the first 10 coordination shells for 10 repeated runs. The error bars are hidden behind the markers, the standard deviation is below 0.005 for all shells. (c) Shows the average enhancement factor for different Clapp configurations and (d) shows the view along the Z-axis of the collapsed unit cell, where all 16 000 atoms are plotted in one cell.

Although full quantitative characterization of texture is possible on NOMAD [39], it is outside of the scope of this paper, which aims to demonstrate the effect of texture on the PDF.

4. Simulation of the texture effect on the pair distribution function

To explore the effects of different textures present in engineering materials on the pair distribution function, the MTEX toolbox [40] was used to generate ODFs for user specified texture components using the *unimodalODF* function, where desired texture was given in Miller indices $\{hkl\}\langle uvw\rangle$ with respect to the crystal symmetry [41]. The Miller notation was used to align with metallurgical nomenclature and to avoid any confusion of rotation angles as MTEX generally applies inverse rotation as compared to Bunge convention. Once the ODF was calculated for the desired texture, a weighting parameter for each of the *hkl* reflections in a desired Q-range (in this case, the maximum Q used was $Q_{max} = 50$ Å^{-1}, which includes 650 reflections) was extracted from the ODF by projecting and integrating pole figures for each reflection. Examples of pole figures and weighting factors are provided in Supplementary information. These weighting factors were applied to a structure factor calculated for a perfect powder, the $F(Q)^0$, to generate a textured structure factor $F(Q)^{tex}$, where the effect of an applied {100}<001> texture is shown in Fig. 6. The strength of the applied texture was defined by texture sharpness, where the generated texture was specified with half-width values in degrees ranging from 45 (weak texture) to 5 (strong texture), where half-width specifies the width of the peak in the pole figure.

$F(Q)^0$ was calculated as a Fourier transform of a $G(r)$ calculated from a box with 250 000 atoms for body-centered cubic (bcc) and 256 000 atoms for face-centered cubic (fcc) using RMCProfile v6.7.9. The large box size was chosen to ensure sharp Bragg peaks with minimal truncation effects from transforming from real space to the $F(Q)$ before applying the texture. Before calculating the structure factor the atoms

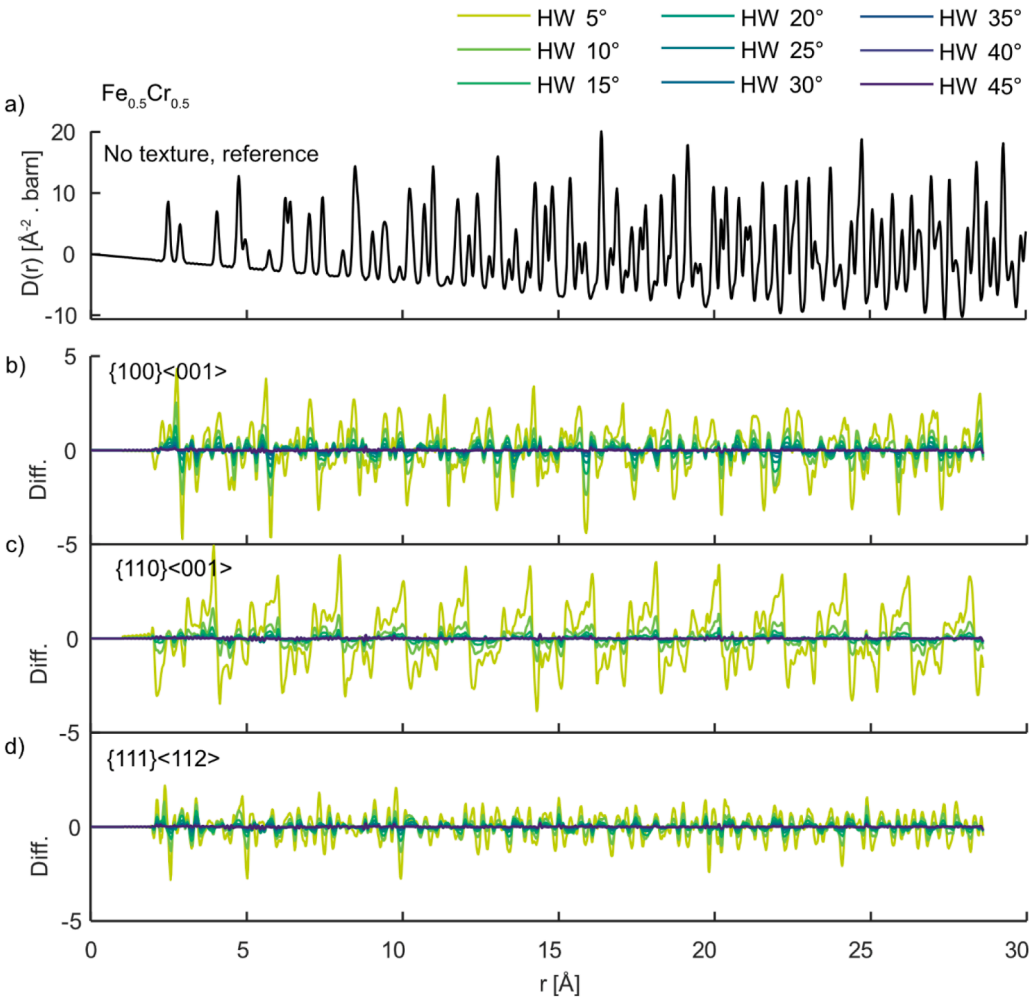

Fig. 9. Difference plots from the $D(r)$ fit of the $Fe_{0.5}Cr_{0.5}$ system, where the PDF is plotted as a reference in (a) and the difference plots from increasingly sharp textures are presented in b-d). (b) {100}<001> texture (c) {110}<001> texture d) {111}<112> texture.

were displaced within the box to mimic thermal vibrations. The displacement was performed using the *gaussdist* command included in the RMCProfile package, with a displacement value $U = 0.08$ Å which randomly shifts atoms within a specified isotropic atomic displacement value according to the Box-Muller method. This slight variation in atomic positions around the mean mirrors the thermal displacement and the resulting decay of scattering intensity at high Q (expressed by the Debye-Waller factor during structural refinement) which allows the $F(Q)^0$ to approach the self-scattering level. This creates a background similar to the experimental background which consists of the diffuse scattering caused by the displacement and the inelastic scattering [42]. To create a textured structure factor $F(Q)^{tex}$, the weighting parameters (derived as described above) were applied to the $F(Q)^0$, where the effect of increasingly strong {100}<001> texture is shown for a bcc structure in Fig. 6. Finally, to see the effect of texture on the PDF the $F(Q)^{tex}$ was Fourier transformed back to real space. Simulations were carried out for the {100}<001>, {110}<001> and {111}<112> textures for bcc, and the effect of different texture types with varying sharpness applied to supercells of pure iron are shown in Fig. 7. The effect of applying texture to fcc materials is provided in the supplementary information for the interested reader. It can be observed that the applied texture contributes to a periodic change of relative peak intensities over the entire r-range.

For both bcc and fcc materials the texture effect is apparent — it gives rise to a change in intensity in PDF peaks. Upon examination of enhanced peaks, we can see that these changes are particularly prevalent in coordination shells where atoms sit on planes coinciding with the reciprocal lattice values of the enhanced texture planes. Differing textures therefore result in different patterning in intensities across the r-range. Further it is worth noting that in some instances it also leads to broadening of some PDF peaks and additional intensity appearing between the bcc peaks. Such peaks would not normally be expected in a PDF pattern and would likely be attributed to the presence of interstitials, minority phases or impurities within the material.

5. Simulation of local order artifacts caused by chosen texture types

To investigate the effect of texture on possible artificial local order artifacts, simulations were set up for an $Fe_{0.5}Cr_{0.5}$ bcc system, with scattering coefficients and partial pairs specified in Table 2.

The untextured and textured structure factors were generated as described in the previous section. For the RMC fitting, a smaller supercell containing 16 000 atoms for bcc and 16 384 for fcc was generated, allowing for fitting the PDF up to 29 Å in real space for both systems (as the algorithm fits the data up to half the size of the box in real space). The simulations were performed by using the $D(r)$ with a weight factor of 0.01 and a $G(r)$ with a weight factor of 10; the ratio between the weight factors favors the fit to the $D(r)$, but through including the $G(r)$ as a dataset both PDF types are directly available at the end of the fitting. Translations and swaps were allowed with a swap probability of 0.3. The iteration limit was set to 500 tested moves per atom (i.e. 8 million moves for bcc and 8.2 million moves for fcc). For each case, the simulations

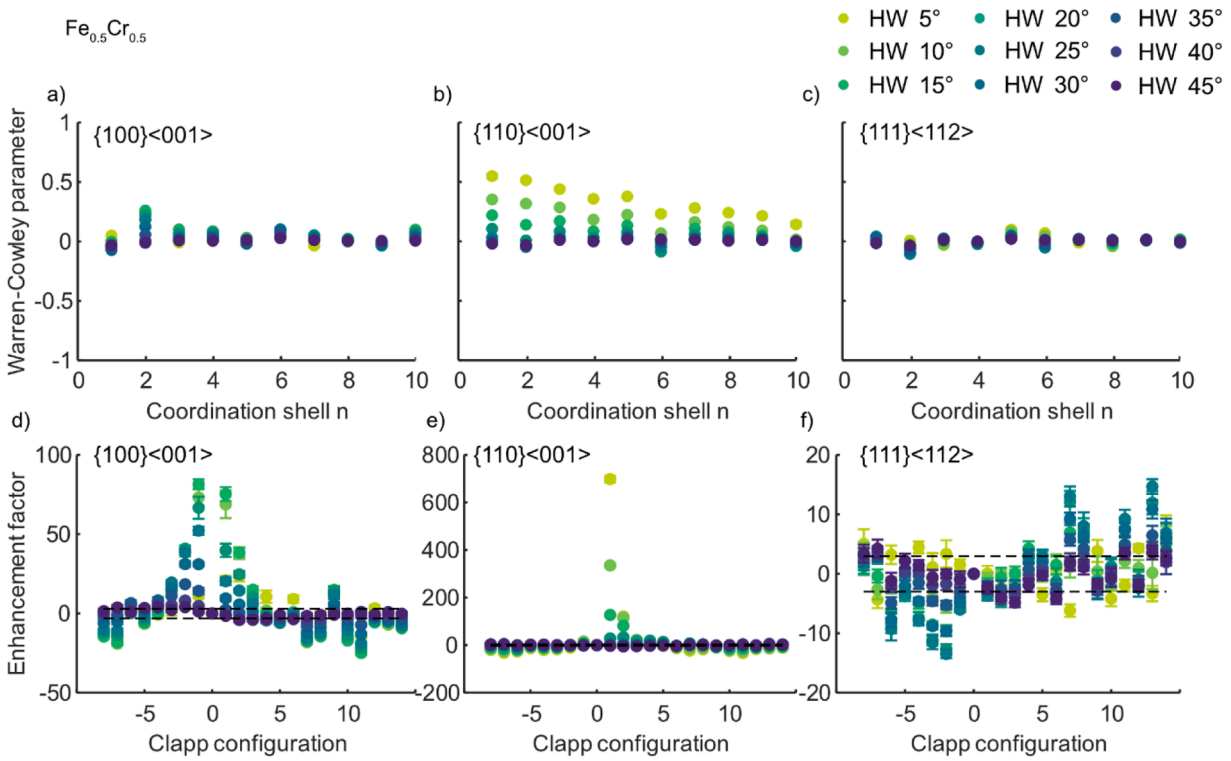

Fig. 10. Average of 10 runs showing the Warren-Cowley parameters for the first 10 coordination shells (a-c) and Clapp configurations enhancement factors (d-f) for different applied textures in the $Fe_{0.5}Cr_{0.5}$ system.

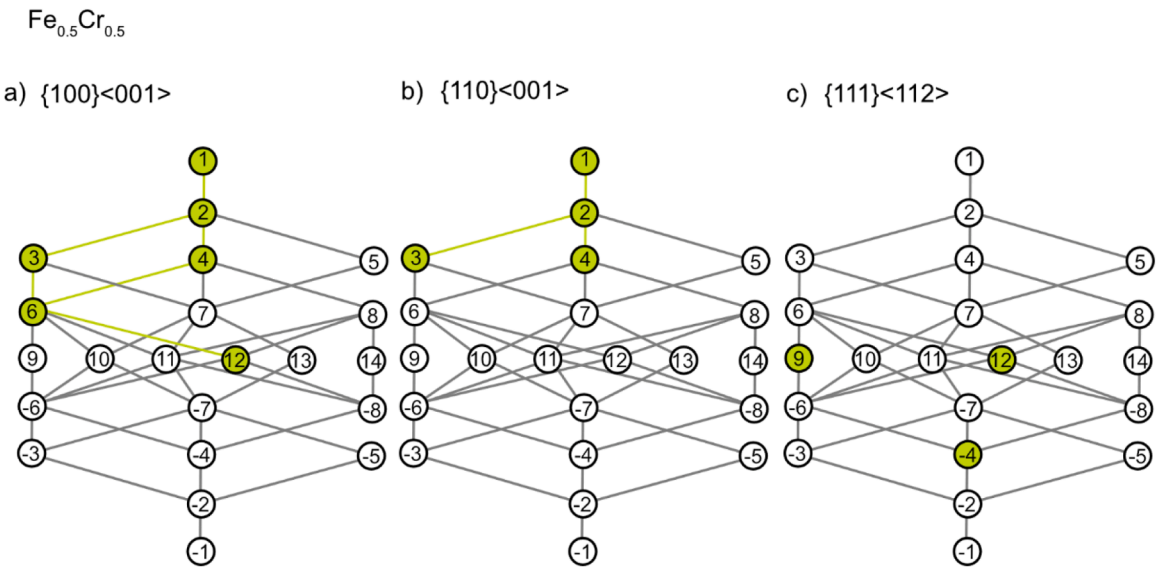

Fig. 11. Degradation diagrams showing the enhanced configurations as a result of fitting strong (half width 5°) texture, (a) {100}<001> texture, (b){110}<001> texture c) {111}<112> texture in $Fe_{0.5}Cr_{0.5}$.

were repeated 10 times to allow statistical analysis.

The resulting boxes at the end of the fit were analyzed by comparing the difference plots between the input data and the resulting model, and by analyzing the atomic arrangements in the box itself with respect to change in the Warren-Cowley parameter and enhancement of any Clapp configurations.

An example of a control run, with no applied texture, is shown in Fig. 8, where the calculated $D(r)$ is presented in Fig. 8a. In Fig. 8b it can be noted that the extracted Warren-Cowley parameters for the first 10 coordination shells are confirming the random arrangements in the cell, fluctuating very close to zero. The same is confirmed in Fig. 8c where the enhancements caused by the finite size of the box are inside and around the bounds of $EF = \pm 3$ for a fully random structure. The collapsed unit cell in Fig. 8d is close to spherical with no apparent distortions, which is expected and caused by the original thermal displacement applied to the $F(Q)$ used to generate the input data.

Starting with the bcc $Fe_{0.5}Cr_{0.5}$ case, the difference plots for all types of textures indicate that the RMC algorithm cannot fit samples with texture, as increasing texture sharpness leads to an increase in the residuals presented in the difference plots (Fig. 9). Extraction of the

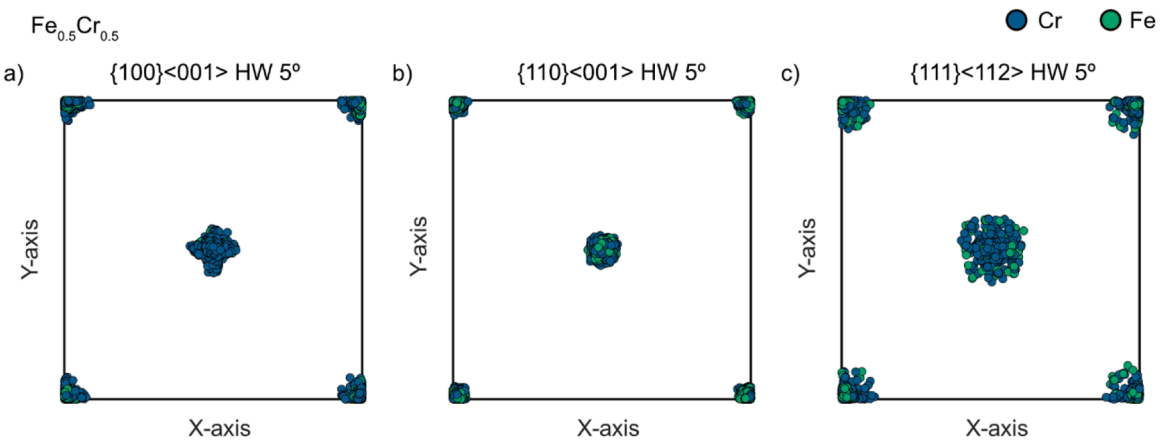

Fig. 12. Distortions on the collapsed supercells of $Fe_{0.5}Cr_{0.5}$ caused by different textures (a) sharp {100}<001> texture (b) sharp {110}<001> texture (c) sharp {111}<112>texture.

Warren-Cowley parameters (Fig. 10a–c) and EFs (Fig. 10d–f) show that different texture types lead to different local order artifacts. For example, the {110}<001> texture leads to clustering artefacts, which can be observed not only by the trend of increasingly positive Warren-Cowley parameters for all coordination shells with increasing texture strength (Fig. 10b), but also by the enhancement of the C1 Clapp configuration (enhancements presented in Fig. 10e, the configuration can be seen in Fig. 1b). Comparing across the strongest texture results, we can extract the enhanced configurations and plot the relation between them in a degradation diagram (Fig. 11). The degradation diagram shows configurations that are similar to each other, where it can be observed that the enhanced configurations are related in some cases (a, b) but not in others (c). Since the enhanced configurations are different for different types of texture, and not always crystallographically related, this might pose another challenge in identification of texture-induced artifacts.

Another challenge in identifying artifacts in the model introduced by texture is the non-systematic distortion introduced in the cell (Fig. 12). It is observed that different textures lead to different distortions of the cell, which are caused by the different ways that the extra intensity is added onto the peaks. For some textures, it only leads to an increase in intensity, while others introduce ripples which broaden the peak, causing the atoms to spread out in the cell (Fig. 12 a and c).

The same trend appears for other compositions with varying contrast, which are provided for the interested reader in the Supplementary information. Similar effects are also observed for the fcc-based materials, also provided in the Supplementary information.

6. Discussion

Both calculations and experimental data clearly show that texture has an influence on the PDF, with simulations showing that texture might introduce artificial local order effects when using a large box model that has been fitted to textured data. This implies that textured samples are not suitable for PDF analysis if texture is not accounted for. However, texture is present in a range of engineering materials fabricated in bulk, e.g. by casting and rolling, materials that also show indication of local order after different heat treatments. Unfortunately, to fully correlate the effects of specific heat treatments to the local structure of a material the characterization needs to be performed for the same heat treatment, and the gas atomization route to prepare powder is not the solution as it would destroy this direct link between processing and structure. This is because the local structure of a material fabricated through powder metallurgy might differ, as it has been emphasized that the local structure of metallic materials is largely dependent on metallurgical history of the sample [12]. Alternative ways of making powder from a previously conventionally processed alloy, for example using filings or milling, might introduce large portions of strain due to the deformation of the surface or contamination of the sample by the filing material. Further, filings could potentially align in a can or capillary in a preferred orientation. Thus, preparation of texture-free metallic powder samples that have been processed by conventional routes might be challenging depending on the materials system. An alternative method of cutting small pieces of a material allow more orientations to appear has been used successfully for total scattering measurements [11] but creating sufficient amounts of material could be tedious, especially for corroding or hard materials that are difficult to cut in a conventional lab setup.

Some of the texture contribution could be avoided by sample rotation such as in the lab scale diffractometer, however, depending on the alignment of the sample this might not eliminate the texture effect, in a similar way as demonstrated for the experimental data in this study (Section 3) where averaging across the few orientations included in the experimental data set was insufficient to create a texture-free data set. Sample rotation might also not be available in some of the desired sample environments such as a furnace or a sample shifter, limiting the availability of this strategy.

For functional materials, such as piezoelectric materials where texture is unavoidable, a correction for the induced anisotropy has been proposed for X-ray scattering by Zhang et al. [43]. The texture correction utilizes a spherical harmonics-based approach, and is applicable to flat panel detectors. For neutron scattering, due to the detector layout this correction is not directly applicable due to the variation in resolution between different detector banks, and due to the simultaneous collection of multiple patterns in ToF experiments. Further adaptation and implementation of this theory is required to make it suitable for ToF multi-bank detectors with varying resolution functions.

The need for characterization of local order arising in materials that are textured from their fabrication route highlights the need to develop a methodology to correct for texture before detailed quantitative analysis of local order from total scattering measurement on textured materials can be applied. A methodology to achieve these corrections is being developed for ToF data and will be the subject of a future publication.

7. Conclusions

In this paper, we have shown experimentally that texture influences the pair distribution function and that texture is not mitigated by merging data from multiple detector banks. Further, we developed a framework to simulate texture effects on a structure factor, which were used to showcase the effect of different texture on the PDF.

Different types of texture have different effects in the resultant PDF,

connected directly to the real-space values of the enhanced texture planes, introducing effects such as change in relative intensity of the peaks, peak broadening and appearance of additional peaks. This can result in texture-induced "artificial order" in the large box model that is fitted to the experimental data. The type of artificial order is dependent on factors including the nature of the texture and the underlying structure across which the order takes place.

To characterize local order phenomena in textured samples using total scattering, it is essential that strategies are implemented to eliminate the texture or its effects in the samples during the experiments (for example by rotation or tumbling of the specimen), or that accurate texture corrections are developed. Without that, our work shows that PDF analysis of materials with preferred orientation will almost certainly give wrong results for local structure data. This insight also implies that texture analysis of samples intended for PDF analysis is necessary.

CRediT authorship contribution statement

Monika Rolinska: Writing – original draft, Visualization, Methodology, Investigation, Formal analysis, Data curation, Conceptualization. **Lewis R. Owen:** Writing – review & editing, Software. **Yuanpeng Zhang:** Writing – review & editing, Software. **Peter Hedström:** Writing – review & editing, Supervision, Funding acquisition. **Matthew G. Tucker:** Writing – review & editing, Supervision, Investigation, Conceptualization.

Declaration of competing interest

The authors declare that they have no known competing financial interests or personal relationships that could have appeared to influence the work reported in this paper.

Acknowledgement

Funding for this work was provided by the Swedish Foundation for Strategic Research (SFF) through the SwedNeSS graduate school (grant number GSn-0008-15). A portion of this research used resources at the Spallation Neutron Source, a DOE Office of Science User Facility operated by the Oak Ridge National Laboratory. The beam time was allocated to NOMAD on proposal number IPTS-27956 and IPTS-29131. The computations were performed on resources provided by the Hillert Modeling Laboratory funded by the Hugo Carlssons Stiftelse för vetenskaplig forskning. The authors acknowledge that this work was conducted in affiliation with the Competence Centre NEutron and X-ray science for industrial Technology transitions (NEXT). The NEXT Competence Centre for Sustainable Industry is financed by Vinnova, Sweden's Innovation Agency [grant number 2023-00553] and its 23 partners from universities, research institutes, large scale research facilities, and companies. Dr. Lewis Owen was supported by the Royal Academy of Engineering (RAEng) the Research Fellowship scheme.

Supplementary materials

Supplementary material associated with this article can be found, in the online version, at doi:10.1016/j.actamat.2026.122122.

References

[1] B.G. Lefevre, A.G. Guy, R.W. Gould, Ordering and the K state in nickel-molybdenum alloys, Trans. Metall. Soc. AIME 242 (1968) 788.
[2] I. Mirebeau, G. Parette, Neutron study of the short range order inversion in Fe1-x Crx, Phys. Rev. B Condens. Matter. Mater. Phys. 82 (2010), https://doi.org/10.1103/PhysRevB.82.104203.
[3] I. Mirebeau, M. Hennion, G. Parette, First measurement of short-range-order inversion as a function of concentration in a transition alloy, Phys. Rev. Lett. 53 (1984) 687–690.
[4] L.R. Owen, E.J. Pickering, H.Y. Playford, H.J. Stone, M.G. Tucker, N.G. Jones, An assessment of the lattice strain in the CrMnFeCoNi high-entropy alloy, Acta Mater. 122 (2017) 11–18, https://doi.org/10.1016/j.actamat.2016.09.032.
[5] Y. Ma, Q. Wang, C. Li, L.J. Santodonato, M. Feygenson, C. Dong, P.K. Liaw, Chemical short-range orders and the induced structural transition in high-entropy alloys, Scr. Mater. 144 (2018) 64–68, https://doi.org/10.1016/j.scriptamat.2017.09.049.
[6] M.M. Nygård, W.A. Sławiński, G. Ek, M.H. Sørby, M. Sahlberg, D.A. Keen, B. C. Hauback, Local order in high-entropy alloys and associated deuterides – a total scattering and reverse Monte Carlo study, Acta Mater. 199 (2020) 504–513, https://doi.org/10.1016/j.actamat.2020.08.045.
[7] J. Zhou, J. Odqvist, L. Höglund, M. Thuvander, T. Barkar, P. Hedström, Initial clustering - A key factor for phase separation kinetics in Fe-Cr-based alloys, Scr. Mater. 75 (2014) 62–65, https://doi.org/10.1016/j.scriptamat.2013.11.020.
[8] H. Thomas, Über widerstandslegierungen, Z. Phys. 129 (1951) 219–232.
[9] L.R. Owen, H.Y. Playford, H.J. Stone, M.G. Tucker, A new approach to the analysis of short-range order in alloys using total scattering, Acta Mater. 115 (2016) 155–166, https://doi.org/10.1016/j.actamat.2016.05.031.
[10] L. Pusztai, R.L. McGreevy, MCGR: an inverse method for deriving the pair correlation function from the structure factor, Phys. B Condens. Matter. 234–236 (1997) 357–358, https://doi.org/10.1016/S0921-4526(96)00986-6.
[11] M.M. Nygård, Ø.S. Fjellvåg, M.H. Sørby, K. Sakaki, K. Ikeda, J. Armstrong, P. Vajeeston, W.A. Sławiński, H. Kim, A. Machida, Y. Nakamura, B.C. Hauback, The average and local structure of TiVCrNbDx (x=0,2.2,8) from total scattering and neutron spectroscopy, Acta Mater. 205 (2021) 116496, https://doi.org/10.1016/J.ACTAMAT.2020.116496.
[12] S.M. Dubiel, J. Cieślak, Short-range order in iron-rich Fe-Cr alloys as revealed by Mössbauer spectroscopy, Phys. Rev. B 83 (2011), https://doi.org/10.1103/PhysRevB.83.180202.
[13] M. Islam, K. Sheriff, Y. Cao, R. Freitas, Nonequilibrium chemical short-range order in metallic alloys, Nat. Commun. 16 (2025), https://doi.org/10.1038/s41467-025-64733-z.
[14] M. Islam, K. Sheriff, R. Freitas, Dislocation-mediated short-range order evolution during thermomechanical processing, Acta Mater. 306 (2026) 121838, https://doi.org/10.1016/j.actamat.2025.121838.
[15] X. Xu, J. Odqvist, M.H. Colliander, S. King, M. Thuvander, A. Steuwer, P. Hedström, Effect of cooling rate after solution treatment on subsequent phase separation during aging of Fe-Cr alloys: a small-angle neutron scattering study, Acta Mater. 134 (2017) 221–229, https://doi.org/10.1016/j.actamat.2017.06.001.
[16] M. Rolinska, G. Spartacus, A. Dahlström, W. Mu, T.G.A. Youngs, J. Odqvist, P. Hedström, Kinetics of phase separation in super duplex stainless steel 2507 revealed by in situ neutron scattering for various intermediate heat treatments, Metall. Mater. Trans. A (2025), https://doi.org/10.1007/s11661-025-07906-1.
[17] K.Y. Nagulin, A.K. Gilmutdinov, A.A. Terentev, Segregation of chemical elements in the volume of powder particles during it's treatment as a method for the production of structurally graded powder materials, Powder Technol. 437 (2024), https://doi.org/10.1016/j.powtec.2024.119516.
[18] Y. Tong, S. Zhao, H. Bei, T. Egami, Y. Zhang, F. Zhang, Severe local lattice distortion in Zr- and/or Hf-containing refractory multi-principal element alloys, Acta Mater. 183 (2020) 172–181, https://doi.org/10.1016/J.ACTAMAT.2019.11.026.
[19] Y. Hu, S. Guo, M.H.ö Colliander, Effect of chemical segregation on accuracy of local lattice distortions determination by pair distribution functions, AIP Adv. 14 (2024), https://doi.org/10.1063/5.0234652.
[20] M. Holscher, D. Raabe, K. Lucke, Rolling and recrystallization textures of bcc steels, Mater. Technol. 12 (1992) 567–575.
[21] R. Manikandan, A.A. Kothari, Y.A. Deshpande, R.A. A, Grain boundary evolution and micro texture development in hot press sintered GRCop alloys, Results Eng. 25 (2025), https://doi.org/10.1016/j.rineng.2025.104471.
[22] J. Al-Lami, T. Dessolier, S.R. Rogers, T. Pirzada, M.S. Pham, Dislocation distribution, crystallographic texture evolution, and plastic inhomogeneity of inconel 718 fabricated by laser powder bed fusion, Adv. Eng. Mater. (2024), https://doi.org/10.1002/adem.202400524.
[23] Z. Gong, S.J.L. Billinge, Atomic pair distribution functions (PDFs) from textured polycrystalline samples: fundamentals, 2018.
[24] A. Cervellino, R. Frison, Texture corrections for total scattering functions, Acta Crystallogr. A Found. Adv. 76 (2020) 302–317, https://doi.org/10.1107/S2053273320002521.
[25] Z. Gong, S. Tao, S.J.L. Billinge, Atomic pair distribution functions from textured polycrystalline samples: fundamentals, Acta Crystallogr. A Found. Adv. 81 (2025) 412–418, https://doi.org/10.1107/S2053273325007387.
[26] P.C. Clapp, Theoretical determination of n-site configuration probabilities from pair correlations in binary lattices, J. Phys. Chem. Solids 30 (1969) 2589–2598.
[27] P.C. Clapp, Atomic configurations in binary alloys, Phys. Rev. B 4 (1971) 255.
[28] D.A. Keen, A comparison of various commonly used correlation functions for describing total scattering, J. Appl. Cryst. 34 (2001).
[29] M.G. Tucker, D.A. Keen, M.T. Dove, A.L. Goodwin, Q. Hui, RMCProfile: reverse Monte Carlo for polycrystalline materials, J. Phys. Condens. Matter 19 (2007), https://doi.org/10.1088/0953-8984/19/33/335218.
[30] Y. Zhang, M. Eremenko, V. Krayzman, M.G. Tucker, I. Levin, New capabilities for enhancement of RMCProfile: instrumental profiles with arbitrary peak shapes for structural refinements using the reverse Monte Carlo method, J. Appl. Crystallogr. 53 (2020) 1509–1518, https://doi.org/10.1107/S1600576720013254.
[31] L.R. Owen, H.Y. Playford, H.J. Stone, M.G. Tucker, Analysis of short-range order in Cu3Au using X-ray pair distribution functions, Acta Mater. 125 (2017) 15–26, https://doi.org/10.1016/j.actamat.2016.11.048.

[32] H.J. Bunge, Texture Analysis in Materials Science, Elsevier, 1982, https://doi.org/10.1016/C2013-0-11769-2.
[33] R.B. Von Dreele, Quantitative texture analysis by Rietveld refinement, J. Appl. Crystallogr. 30 (1997) 517–525.
[34] U.F.. Kocks, H.R. Wenk, C.N.. Tomé, Texture and Anisotropy : Preferred Orientations In Polycrystals And Their Effect On Materials Properties, Cambridge University Press, 1998.
[35] H.R. Wenk, L. Lutterotti, S.C. Vogel, Rietveld texture analysis from TOF neutron diffraction data, Powder Diffr. 25 (2010) 283–296, https://doi.org/10.1154/1.3479004.
[36] R.K. Ray, J.J. Jonas, Transformation textures in steels, Int. Mater. Rev. 35 (1990) 1–36.
[37] J. Neuefeind, M. Feygenson, J. Carruth, R. Hoffmann, K.K. Chipley, The nanoscale ordered materials diffractometer NOMAD at the spallation neutron source SNS, Nucl. Instrum. Methods Phys. Res. B 287 (2012) 68–75, https://doi.org/10.1016/j.nimb.2012.05.037.
[38] B.H. Toby, R.B. Von Dreele, GSAS-II: The genesis of a modern open-source all purpose crystallography software package, J. Appl. Crystallogr. 46 (2013) 544–549, https://doi.org/10.1107/S0021889813003531.
[39] N.E. Peterson, J.R. Einhorn, C.M. Fancher, J.R. Bunn, E.A. Payzant, S.R. Agnew, Quantitative texture analysis using the NOMAD time-of-flight neutron diffractometer, J. Appl. Crystallogr. 54 (2021) 867–877, https://doi.org/10.1107/S1600576721003022.
[40] F. Bachmann, R. Hielscher, H. Schaeben, Texture analysis with MTEX- Free and open source software toolbox. Solid State Phenomena, Trans Tech Publications Ltd, 2010, pp. 63–68, https://doi.org/10.4028/www.scientific.net/SSP.160.63.
[41] R. Hielscher, H. Schaeben, A novel pole figure inversion method: specification of the MTEX algorithm, J. Appl. Crystallogr. 41 (2008) 1024–1037, https://doi.org/10.1107/S0021889808030112.
[42] K. Page, C.E. White, E.G. Estell, R.B. Neder, A. Llobet, T. Proffen, Treatment of hydrogen background in bulk and nanocrystalline neutron total scattering experiments, J. Appl. Crystallogr. 44 (2011) 532–539, https://doi.org/10.1107/S0021889811001609.
[43] G. Zhang, H. Liu, J. Chen, H. Lin, N. Zhang, A spherical harmonics method for processing anisotropic X-ray atomic pair distribution functions, J. Appl. Crystallogr. 56 (2023) 275–281, https://doi.org/10.1107/S1600576723000109.